Characterization study of the CsI(Tl) detector array

by

Corwin Trottier

A THESIS SUBMITTED IN PARTIAL FULFILMENT OF
THE REQUIREMENTS FOR THE DEGREE OF

BACHELOR OF SCIENCE

in

Honors Physics

(Department of Physics and Astronomy, Dr. R. Kanungo supervising faculty)

. . . . . .
. . . . . .
. . . . . .
. . . . . .
. . . . . .

SAINT MARY'S UNIVERSITY

April 28, 2013

Abstract

Characterization study of the CsI(Tl) detector array, by *Corwin Trottier*, submitted on April 28, 2013:

The ISAC Charged Particle Spectroscopy Station (IRIS) at TRIUMF, Vancouver, Canada uses CsI(Tl)—a 16 component detector array composed of thallium-doped cesium iodide—for high resolution study of nuclear reactions. Each CsI(Tl) detector was characterized by studying its response and determining its Q-value resolution for scattering reactions. The elastic scattering of $p(^{18}O, p)^{18}O$ among similar higher-energy inelastic reactions were examined during the calibration process. Data from several experimental runs were compared to kinematics curves to calibrate the energy response of each CsI(Tl) sector. Elastic and inelastic Q-value peaks were corrected for dependence on scattering angle and measured for resolution.

CsI(Tl) is an inorganic scintillator crystal, which is coupled to a photodiode. The annular-type detector array consists of 16 identically designed sectors. Each sector was characterized separately in order to describe the detector array as a whole. In general, the characterized CsI(Tl) detector will detect hydrogen isotope reaction products that were scattered from a target of similar atomic structure. Motivation for this study includes the future use of the CsI(Tl) detector in nuclear reactions involving radioactive ion beams at IRIS. These reactions can provide further understanding of the nuclear force, shell structure and general theory of unstable exotic nuclei.

Contents

Abstract 2

Contents 3

List of Figures 5

List of Tables 6

1 Introduction 7

1.1 Exotic Nuclei 7

1.2 Nuclear Reactions 9

1.3 Particle Detectors 12

2 IRIS Facility 15

2.1 Research and Motivation 15

2.2 Detector Specifications 16

2.3 Beam Specifications 18

3 Data Analysis 20

3.1 Theoretical Framework 20

3.2 Elastic Scattering: Energy Calibration 23

3.3 Inelastic Scattering: Q-Value Resolution 27

4 Discussion 34

4.1 Energy Calibration of CsI 34

4.2 Angular Correction 35

4.3 Detector Resolution 39

5 Conclusions 44

Bibliography 46

List of Figures

3.1 Kinematics $(E, \Delta E)$ for $p(^{18}O, p)^{18}O$ with a $4.1 MeV/u$ beam 22

3.2 Scatterplot of $(ADC, \Delta E)$ with the $4.1 MeV/u$ beam 24

3.3 Superposition of Figure 3.1 with experimental data 24

3.4 Energy calibration of CsI sector 12 using equation (3.1) 26

3.5 Superposition of data and kinematics (θ, E) with a $4.1 MeV/u$ beam . 27

3.6 Superposition of data and kinematics (θ, E) with the $11.8 MeV/u$ beam 28

3.7 Scatterplot of $(E, \Delta E)$ in keV with the $11.8 MeV/u$ beam 29

3.8 Kinematics $(E, \Delta E)$ for $p(^{18}O, p)^{18}O^*$ with the $11.8 MeV/u$ beam . . 30

3.9 Scatterplot of Q-value (keV) versus θ (°) 30

3.10 Scatterplot of Q_{new} (keV) versus θ (°) after correction 31

3.11 Scatterplot of Q_{new} (keV) versus θ (°) after second correction 32

4.1 Calibration plot with data only from individual rings 13 to 16 36

4.2 Calibration plot using data from four groups of four rings 37

4.3 Q-value histogram peak near $Q = -5.255$ MeV for the CsI array . . . 40

4.4 Histogram of CsI sector 10 shifted from the $Q = -1.982$ MeV peak . 41

4.5 Histogram of CsI sector 3 skewed from the $Q = -1.982$ MeV peak . 42

4.6 Histogram of CsI sector 1 around the $Q = -1.982$ MeV peak 43

4.7 Energy resolution of CsI sectors at $Q = 0$ and $Q = -1.982$ MeV peaks 43

List of Tables

3.1 YY1 ring positions and corresponding scattering angles 21

3.2 Mean energy of ring groups 25

3.3 Gain determined by linear regression 26

3.4 Quadratic fit parameters for $Q = -1.982$ MeV 31

3.5 Quadratic fit parameters for $Q = -5.255$ MeV 32

3.6 FWHM resolution in units of MeV for different Q_{new} peaks 33

4.1 Mean Q-value for different Q_{new} peaks 38

4.2 Q-value histogram data for the first excited state 41

Chapter 1

Introduction

1.1 Exotic Nuclei

The number of known unstable nuclear isotopes vastly outnumbers the stable isotopes in the chart of nuclides. Many of these unstable isotopes are involved in neutron and proton capture reactions in stellar nucleosynthesis [1], but are not created or found naturally on Earth. Therefore, many properties of neutron and proton rich nuclei are unknown or narrowly understood. Studying the most exotic nuclei is important in understanding processes by which heavy nuclei form. Furthermore, by conducting experiments with nuclei in the unstable regions of the chart of nuclides, researchers can gain insight into fascinating properties of rare isotopes.

Reactions involving neutron-rich isotopes have been gaining popularity since the discovery by I. Tanihata et al. (1985) of what are now known as halo nuclei [2]. These exotic nuclei exist around drip lines, which define the borders of bound nuclei in the chart of nuclides. Nuclei with large ratios of protons to neutrons tend to be less tightly bound. Highly neutron-rich nuclei have decreased neutron separation energy, resulting in a low density extension of the neutron distribution and a higher interaction cross section [3]. This phenomenon can lead to neutron skin forming around the nucleus, and for extreme cases, one or more neutrons can be identified in halos outside the nucleus [4]. Proton halos also exist in nuclei near proton drip lines

on the other side of the chart of nuclides but are less abundant due to the Coulomb repulsion [5].

Exotic nuclei around the drip lines are studied using radioactive ion beams (RIBs). Many different kinds of reactions using RIBs have been performed in order to study density distribution, energy levels and excitation of neutron-rich nuclei [5, 6]. Nuclear orbitals and spin states of halo nuclei can be measured using heavy RIBs in transfer reactions with hydrogen isotopes (d, p) and (p, d). Scattering reactions with proton targets—as in this thesis—have also been used to study the structure of the halo itself using high intensity RIBs [2]. It has been found that exotic nuclei experience changes in shell structure and even show a new neutron magic number of stability around $N = 16$, while neighbouring accepted magic numbers disappear [6, 7]. RIBs have made the study of many unknown rare isotopes possible. Further progress on heavier ion beams will likely extend the list of known halo nuclei as well the collective knowledge of all properties of exotic nuclei.

Researchers have only begun to study halo nuclei in depth; there is still much to explore. There is a wealth of knowledge on very unstable nuclei waiting to be tapped in this field. Studying exotic nuclei may also contain key information pertaining to nucleosynthesis environments, such as within supernovae and neutron stars. Nuclear reactions involving neutron-rich nuclei are conducted at facilities like IRIS with hopes to continue to produce and study more exotic and important isotopes.

1.2 Nuclear Reactions

Nuclear reactions are important and necessary for determining properties of the nuclei involved. Particle beams such as RIBs can be directed toward targets in which the projectile nuclei collide with the target nuclei producing different or altered reaction products. The reaction products can be examined using detectors to study the parameters of the collision and determine other properties about the incident nuclei. Charged particle spectroscopy reactions are frequently carried out in inverse kinematics, where a radioactive ion beam is incident upon a lighter target [8].

Direct nuclear reactions involve a short time scale of interaction between the projectile and the target. During this time, interaction occurs at or near the surface of the participating nuclei and may result in a transfer of nucleons or an excited energy state of one of the reaction products. Direct reactions involving rare isotope beams are of importance for determining excited states of reaction products as well as physical and shell structures of exotic nuclei. A general direct reaction can be represented by the notation $A(B,C)D$, where A represents the stationary target, B is the projectile, C is the detected target-like ejectile, and D is the heavier reaction product.

Basic direct reactions include elastic scattering and inelastic scattering. In both reaction channels the composition of the two nuclei are not altered during the collision. The only exception is that inelastic scattering involves the excitation to a higher energy level in one of the reaction products. Extra energy must be added to the system in inelastic collisions to allow for the excitation energy jump. The Q-value of a reaction measures the amount of energy released or absorbed by the system, as a positive or negative value respectively. The excitation energy associated with an

inelastic collision corresponds to the Q-value of that reaction.

The Q-value of a scattering reaction is calculated as follows:

$$Q = E_b \left(\frac{M}{M_2} - 1 \right) + E_L \left(\frac{m}{M_2} + 1 \right) - 2\sqrt{MmE_L E_b} \frac{cos\theta}{M_2}, \tag{1.1}$$

where E_L is the total energy of the detected light reaction product after scattering, E_b is the initial total energy of the beam and θ is the scattering angle. M and m are the masses of the the beam nucleus and target nucleus respectively. M_2 is the mass of the heavy product nucleus. In scattering reactions $M = M_2$.

Direct reactions also include breakup and transfer reactions, which involve the release or exchange of nucleons upon interaction of the projectile and target nuclei. A breakup reaction is a three-body reaction, which splits one of the incident nuclei upon interaction, resulting in three reaction products. Pickup reactions such as (p, d) and stripping reactions such as (d, p) are transfer reactions that may show insight into the properties of some rare isotopes by indirectly studying the neutron and proton capture reactions [9]. These properties include determining the spin of the heavy reaction product if the spin of the incident beam is known. Nuclear orbitals and changes in magic numbers can also be studied with these reactions.

Capture reactions occur when a nucleon is absorbed by another nucleus upon interaction. Elements of higher atomic number are produced in the case of proton capture, while heavier isotopes are produced by neutron capture (n, γ). If an unstable heavy isotope is produced by (n, γ), then the nucleus is able to decay by electron emission (β^-), losing one neutron and gaining a proton [10]. Nucleosynthesis processes

that depend on these reactions are the s-process and the r-process, the latter requires environments with high neutron densities [11]. The progression of these processes is responsible for the formation of the majority of naturally occurring neutron-rich elements above atomic number $A \approx 70$.

The s-process is directed by a slow rate of (n, γ) compared to the rate of (β^-). When (n, γ) produces an unstable nucleus, the nucleus will go through beta decay until it reaches a stable state. These reactions typically take place cyclically in massive stars of moderate neutron density and temperature. This causes heavier nuclei to form along the stability line in the neutron-rich region of the chart of nuclides.

The r-process occurs in regions of very high neutron density (about 7-8 times that of protons [11]) where (n, γ) occurs at rapid time scales compared to (β^-). Unstable nuclei may continue to capture more neutrons until the cross section for (n, γ) reaches equilibrium with (γ, n). At this point, the nucleus will not make progress in either gain or loss of nucleons until (β^-) takes over. This process produces heavy nuclei beyond the capabilities of the s-process because it follows unstable neutron-rich nuclei near the drip line instead of following the stability line. The r-process is not very well understood in general but it is an example of the importance of studying unstable neutron-rich nuclei. Proposed atmospheres for the r-process include explosive environments around core-collapsed supernovae [12, 13]. Newly created neutron stars may eject very hot and neutron-rich wind, which is thought to provide ideal conditions for the r-process [14]. Direct reaction experiments at IRIS will involve neutron-rich nuclei that may have involvement in the r-process. These experiments can help understand the role of these nuclei in nucleosynthesis.

1.3 Particle Detectors

One of the most useful methods of detection and spectroscopy of charged particles involves the use of scintillation. This study involves charged reaction products, which can interact with scintillators to produce optical photons. A successful detector must convert all of the energy in the charged reaction product into optical energy. This characteristic is given by the linear stopping power of the scintillator. In any absorber, the stopping power relates the energy absorbed by the target material to the distance travelled by the charged particle (x). The rate of the particle's energy loss is given by:

$$S = -\frac{dE}{dx}. \tag{1.2}$$

For charged particles such as the high energy hydrogen isotopes detected in this thesis, the specific energy loss in a detector is given by the Bethe formula [15]:

$$-\frac{dE}{dx} = \frac{4\pi e^4 z^2}{m_0 v^2} NB, \tag{1.3}$$

where the stopping number for relativistic particles is

$$B = Z\left(ln\left[\frac{2m_0v^2}{I}\right] - ln\left[1 - \left(\frac{v}{c}\right)^2\right] - \left(\frac{v}{c}\right)^2\right). \tag{1.4}$$

In equation (1.3), m_0 is the electron rest mass and v is the particle's velocity, while ze represents its charge. In equation (1.4), c is the speed of light in vacuum and I is the average excitation and ionization potential of the absorber. The second and

third terms in equation (1.4) may be left out in the consideration of non-relativistic particles. Substituting for B in equation (1.3) reveals that the stopping power depends dominantly on the factor NZ, which represents the number density of electrons and atomic number in the absorber.

The preceding equations indicate that the stopping power of a material increases with its atomic number and density. Thallium activated cesium iodide, CsI(Tl), is an inorganic scintillator with relatively high density and effective atomic number, which makes it an ideal stopping detector [16]. CsI(Tl) is commonly used for this purpose as the final detector in telescope arrays [17], and for mass and charge detection of heavy ions [18, 19]. Other advantages of this scintillator include low hygroscopicity, high energy resolution, and very high light output [20]. The stopping power, among other useful qualities of CsI(Tl), makes it ideal for total energy detection of high-energy particles.

The CsI(Tl) crystal is composed of a cesium iodide lattice with impurities of thallium, known as activators. When a charged particle interacts with the crystal it loses energy and may excite an electron to a higher energy level. The purpose of the thallium activator is to produce an intermediate energy level for the de-excitation of the electron [15]. This allows the excitation energy of the electron to be released as optical photons, producing scintillation light. This process is not entirely efficient but the energy deposited into the scintillator crystal is proportional to the number of optical photons.

When a scintillator is coupled to a semiconductor photodiode, the optical photons produced by scintillation are turned into electron-hole pairs in the photodiode.

Production of electron-hole pairs close enough to the semiconductor's depletion region results in the generation of voltage output from the photodiode. The net effect of all interactions is a direct proportionality between the energy deposited in the CsI(Tl) detector and the number of electron-hole pairs. Thus, through the use of both scintillation and photo-detection, the energy of a charged reaction product can be determined by measuring the output voltage from the detector.

Photodiodes generally have high quantum efficiency; when they are optically coupled with certain scintillators, a high-energy resolution can be achieved. The CsI(Tl) scintillator crystals, which are the subject of this study, have the best signal to noise ratio in this respect [21]. Also, photons emitted from the CsI(Tl) crystal have a peak wavelength of 550 nm, which introduces a convenient compatibility with silicon semiconductor photodiodes [19, 21]. A silicon PIN photodiode of type S3584-08 from Hamamatsu [22] was used in this study and will allow the IRIS facility to analyze reaction products with high energy resolution and high efficiency in future experiments.

Chapter 2

IRIS Facility

2.1 Research and Motivation

TRIUMF hosts a number of facilities used to create, separate, and accelerate radioactive ion beams. Known jointly as the Isotope Separator and Accelerator (ISAC) facility, these facilities generate secondary beams by colliding proton beams from the main cyclotron with target nuclei [23, 24]. Different ions generated in this manner are separated for use in various experiments. High energy RIBs from the ISAC-II facility are sent to the ISAC Charged Particles Spectroscopy Station (IRIS), which will use the beams in nuclear reactions involving isotopes to study exotic nuclei.

Research at IRIS is motivated by a desire to understand nuclear orbitals and nucleon magic numbers in isotopes far from the stability curve. There is no well-defined model that describes what is actually observed in these regions, but IRIS is dedicated to studying them experimentally. IRIS aims to gather information on the angular momentum, spin, and energy levels of unstable nuclei, which will expand current understanding of the shell structure of exotic nuclei [9]. Understanding the mechanisms behind nucleosynthesis near the nucleon drip lines is also a driving factor for this facility. Much of the high resolution detection at IRIS will use the CsI(Tl) detector array studied in this thesis.

General research at IRIS will involve the study of unstable and rare isotopes via

charged particle spectroscopy. Rare isotope beams from ISAC-II will be fired at low-Z targets to initiate reactions in inverse kinematics. Detectors may be set up beyond the target and also upstream from the target depending on the reaction kinematics. Desired transfer and inelastic reaction channels will be selected by varying the beam's energy. Furthermore, specific reaction channels can be identified by examining the energy loss of reaction products as recorded by each detector.

2.2 Detector Specifications

This section describes the detectors from which data used in this thesis were recorded. Specifications outlined in this section were adapted from ref. [9].

The IRIS facility uses a $\Delta E - E$ telescope setup in order to map the energy and scattering angle of reaction products. This telescope employs a YY1 type silicon semiconductor detector manufactured by Micron Semiconductor Ltd. [25] followed by a CsI(Tl) detector. Particles will pass through a telescope's detectors in series before depositing their remaining energy in the final detector. The final detector measures the residual energy, E, after the particle experiences energy loss, ΔE, in the previous detector or detectors. The setup in the IRIS facility is used to detect the lighter reaction products that travel downstream from the target. Furthermore, the $\Delta E - E$ telescope design offers the ability to distinguish between reaction products by their mass and charge [26]. For instance, plotting the relationship between energy loss and residual energy can show patterns followed by reaction products of different mass and charge.

IRIS uses the YY1 silicon strip detector as the ΔE component of the telescope.

YY1 is a single sided annular array consisting of 8 wedge-shaped sectors. Each sector has 16 concentric detector rings allowing YY1 to measure the energy loss of the light reaction products at different scattering angles θ. The interior ring has an inner radius of 5.0 cm and an outer radius of5.5 cm. The strip pitch of each subsequent ring is also 0.5 cm. Thus, the outer radius of the 16th ring is 13.0 cm. The dimensions of the detector give the following expression for calculation of scattering angles:

$$\theta = tan^{-1}\left(\frac{r}{d}\right), \tag{2.1}$$

where r is the radial distance from the center of the array and $d = 30.0$ cm is the distance between the YY1 detector and the target. This configuration can detect ejectiles at lab angles between 9.46° and 23.43°. This range of angles includes some of the most energetic ejectile particles without detecting the recoiled heavy nuclei, which are scattered at smaller angles.

When a particle travels through YY1 it experiences energy loss, which depends on the thickness of the detector. A particle moving through a medium at an angle θ experiences an effective thickness, η_{eff}, which is simply given by trigonometry:

$$\eta_{eff} = \frac{\eta}{cos\,(\theta)}. \tag{2.2}$$

The YY1 detector has a thickness of $\eta = 100$ μm thick. This silicon detector is not sufficient in thickness or stopping power to absorb all of the energy from the ejectiles. These particles pass through the silicon detector, losing some energy, and then proceed toward the CsI(Tl) detector.

The telescope component that measures residual energy, E, is the thallium-doped cesium iodide detector array (CsI). This is also an annular array, which has 16 wedge-shaped sectors. The CsI(Tl) detector was designed and positioned so that ejectiles passing through any one sector of the YY1 detector will subsequently hit one of two adjacent CsI sectors. Therefore, each sector of YY1 corresponds to two CsI sectors. The CsI detector is much thicker than YY1 at 12 mm. Greater detector thickness along with the high stopping power of CsI allows this detector to register the remaining energy for beam energies used in this study.

Analog-to-Digital converters (ADCs) are used to convert the electrical pulses from each detector into digital signals. There are ADCs for each ring in each section of the YY1 detector for a total of 128 ADCs. The CsI detector also has a total of 16 ADCs, one for each sector. Each successful event will produce a signal on one of the 16 YY1 rings as well as on a corresponding CsI sector. Thus, the signal can be matched to one of 256 detector segments in the telescope array. Consequently the $\Delta E - E$ telescope can be used to characterize the energy response and angular dependence of that response for each CsI sector individually.

2.3 Beam Specifications

This study focuses on direct reactions involving an ^{18}O isotope beam incident upon protons in a polyethylene, (CH2)n, target. The target has a thickness of 350 μg/cm^2, which contributes to the energy loss of the reaction but is immaterial to the calibration and characterization of the detector array. Two sets of experimental data were analyzed in this thesis, using the same ion beam and target configuration but with

beams of differing energy.

The first set of data was used to calibrate the energy response of the CsI detector. A beam energy of 4.1 MeV/u (Mega electronvolts per nucleon) was used for this purpose. The low beam energy put emphasis on the elastic scattering reaction $p(^{18}O, p)^{18}O$. Data corresponding to this reaction channel were analysed and used for the energy calibration of CsI.

The second set of data was collected using a beam energy of 11.8 MeV/u. This beam energy opened higher reaction channels that were not present in the lower-energy data set. The inelastic scattering reaction $p(^{18}O, p)^{18}O^*$was examined and used to further analyze the energy response of the CsI detector. The resolution of the Q-value peaks in certain scattering reactions was determined for each sector in the detector using this set of data.

Chapter 3

Data Analysis

3.1 Theoretical Framework

Data used in this thesis were collected from the ADCs at the IRIS facility during several experimental runs. Consideration of energy and momentum conservation for each reaction provided visual and numerical assistance for the data analysis. Calculations for this section were based on the reaction kinematics and the interaction of the relevant particles with each detectors. Energies detected by both the YY1 detector and the CsI detector at various scattering angles were calculated. These calculations were used to identify the relevant reaction channels throughout the data and set the standard for calibration purposes.

Scattering angles that correspond to different rings in the YY1 detector were calculated using equation (2.1). The dimensions of each ring segment within YY1 are displayed in Table 3.1 along with the corresponding scattering angles—those for which scattered nuclei strike the center of each ring. These angles were calculated from the detector dimensions by using equation (2.1). In general, particles striking the middle of a ring will provide an average value of the energy distribution identified by that detector ring. For this reason, all calculations and data analysis will be conducted using the angles in Table 3.1.

Ring	Radial distance (cm)	Scattering angle ($^\circ$)
1	5.2	9.83
2	5.7	10.76
3	6.2	11.68
4	6.7	12.59
5	7.2	13.50
6	7.7	14.40
7	8.2	15.29
8	8.7	16.17
9	9.2	17.05
10	9.7	17.92
11	10.2	18.78
12	10.7	19.63
13	11.2	20.47
14	11.7	21.31
15	12.2	22.13
16	12.7	22.95

Table 3.1: YY1 ring positions and corresponding scattering angles

The first reaction that was analyzed in this thesis was the elastic scattering of $p(^{18}O, p)^{18}O$. The reaction takes place at the polyethylene target described in section 2.3. The reaction products are scattered and remain unchanged except for their momentum and energy, and of course the scattering angle of the ejectile proton. The energy transferred to the ejectile proton was calculated for each angle with the Catkin kinematics calculator [27]. The energy loss from the particle's travel through the target was also calculated. Energy loss calculations were performed with the LISE++ physical calculator [28]. The energy loss in the target is needed to determine the energy loss in subsequent detectors. However, energy loss from the thin target is negligible comparable to the residual energy of the CsI detector and can be omitted for purposes of energy calibration.

The theory of stopping power suggests that oxygen nuclei in the beam will lose energy faster than the scattered proton as they pass through the target. The energy loss in the target can vary depending on where the collision occurs. The average oxygen nucleus travelling through the target can be thought to collide with a proton around the middle of its journey. This establishes average energy loss for the 16

scattering angles displayed in Table 3.1. With this in mind, the energy loss in the target must be calculated before and after the collision. The thickness of the target is very small compared to the distance to the YY1 detector, so the scattering angles will correspond to the established rings correctly, regardless of where the collision takes place in the target.

The most important consideration for the kinematics model is the proton's energy loss in the YY1 detector, ΔE, and its remaining energy, E, detected by CsI. The reaction kinematics shows an inverse relationship between the scattering angle of ejectiles and their total kinetic energy. Furthermore, there is less energy loss for particles travelling at smaller angles through YY1 due to lesser effective thickness. Thus, the kinematics model shows that the inner edge of each detector detects particles with the highest energy.

This model provides theoretical values of E and ΔE for all 16 rings as well as upper and lower boundaries. The interdependence between a proton's modelled residual energy and energy loss in YY1 is shown in Figure 3.1 for the low-energy experiment. Experimental data can be compared to this relationship to facilitate the identification of the reaction channel and products. This model also provides the energy values for calibration of the CsI detector.

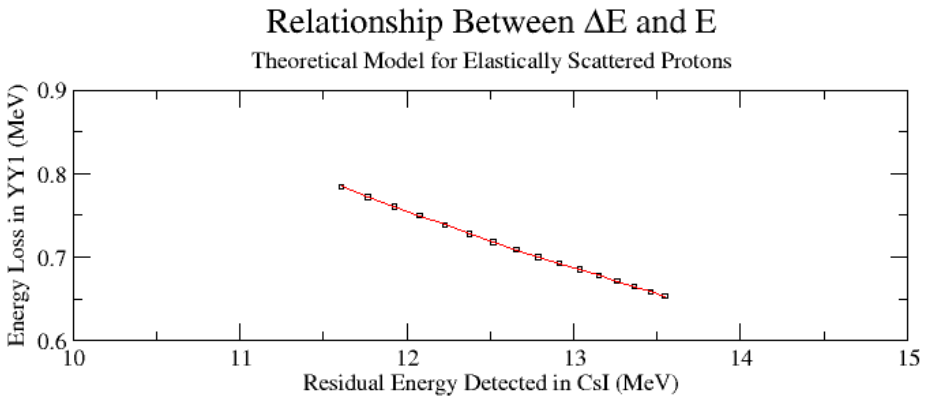

Figure 3.1: Kinematics $(E, \Delta E)$ for $p(^{18}O, p)^{18}O$ with a $4.1 MeV/u$ beam

3.2 Elastic Scattering: Energy Calibration

Every time a particle was detected by the YY1 or CsI detectors a corresponding event was recorded. Each event contained the following information relevant to the data analysis for each detector: the ID number of the ADC that recorded the strongest signal, along with a numerical value of that signal given by the ADC. With the proper detector calibration this amounts to knowing how much energy was recorded by each detector for a specific reaction event. The effect of all events shows the energy distribution recorded across the entire detector array by separate detectors.

The residual energy is determined from the signal strength of the CsI ADC (ADC) by applying a simple linear calibration equation:

$$E = gain \times (ADC - ped)\,, \tag{3.1}$$

where $gain$ is the gain of an individual detector and ped is the pedestal, a coefficient to account for the shift in ADC from background offset. Energy calibration had previously been completed for the YY1 detector (ΔE). This section describes the data analysis from which values for the gain and pedestal were calculated for each sector of the CsI detector array.

Data from five experimental runs with the beam's energy at 4.1 MeV/u were included in this analysis. Furthermore, only the elastic scattering of protons were examined for the energy calibration. Protons were identified by using the $\Delta E - E$ system, where ΔE was known and E was not yet calibrated. Figure 3.2 shows a scatterplot of the data from all five runs with ΔE along the vertical axis and ADC along the horizontal axis, representing residual energy. The band of protons was compared to the curve in Figure 3.3 to verify the particles of correct charge and mass.

The elastic proton band was isolated and used to create conditions for the selection of protons striking specific locations on the telescope array. This was done by pairing

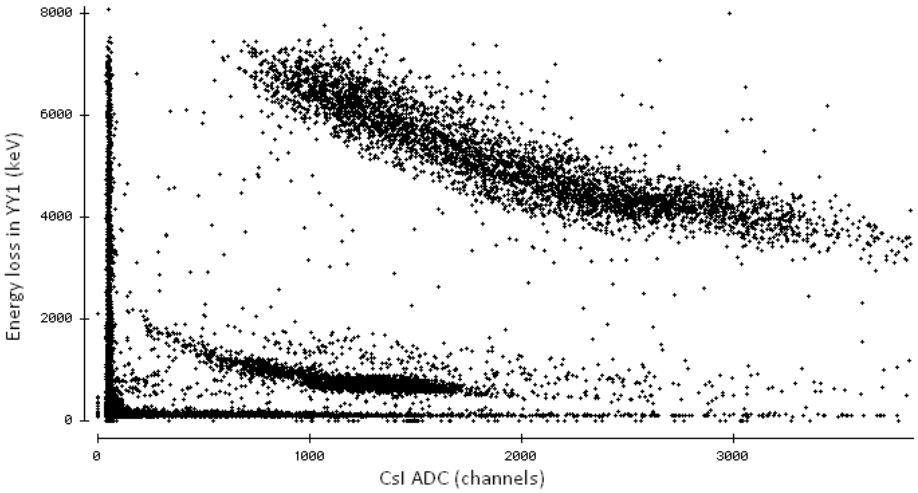

Figure 3.2: Scatterplot of $(ADC, \Delta E)$ with the $4.1 MeV/u$ beam

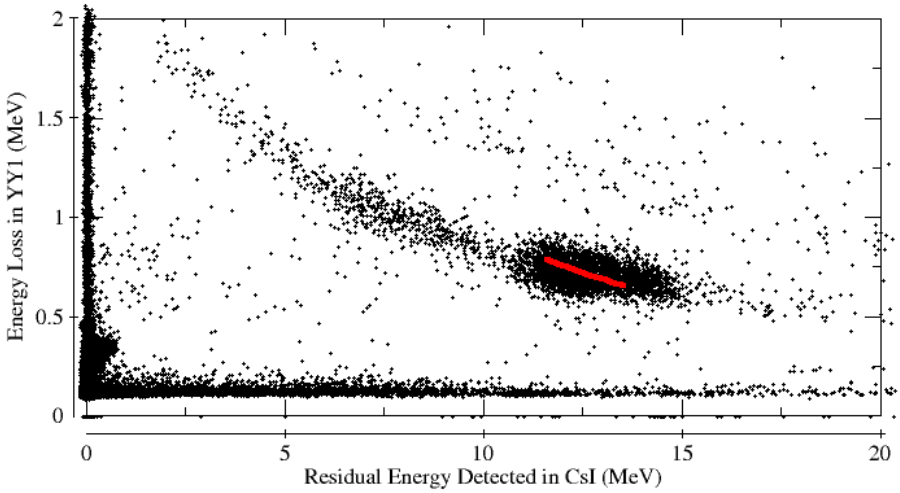

Figure 3.3: Superposition of Figure 3.1 with experimental data

the ID values of CsI and YY1 for each event. Data could then be examined for any combination of the 16 CsI sectors and the 16 YY1 rings. Furthermore, false events were reduced by ensuring that recorded ID values for both detectors corresponded to back-to-back sectors. Lastly, each of the 16 CsI sectors was treated separately so that they were each calibrated for gain and pedestal values individually.

Data from protons detected by the four inner YY1 rings were isolated for each CsI sector. Similarly, the next four rings were grouped together, and the next four, and the last four. The CsI ADC values of these data were plotted into four separate histograms. The resulting plots were fitted with a Gaussian distribution in order to

determine the peak ADC channel. The peak value of ADC from the four inner rings corresponds to the average residual energy E—detected by the selected CsI sector—of protons that passed through rings 1-4 of YY1. This procedure gives four values of E corresponding to four different scattering angles along CsI.

The kinematics model is used to compare the average ADC channel to the energy values that should be recorded at the corresponding scattering angles. Theoretical values of E were taken as the average of the residual energy values passing through each four-ring segment. Table 3.2 summarizes these values, which were averaged from data in Table 3.1. This procedure gives four ordered pairs (ADC, E) for each CsI sector, which can be plotted and fit with a linear regression. The coefficient (a) and constant (b) determined by the fit correspond to the gain and pedestal respectively.

$$E = a \times ADC + b. \tag{3.2}$$

By comparing equations (3.1) and (3.2) it follows that

$$gain = a, \qquad ped = -\frac{b}{a}. \tag{3.3}$$

Ring Group	Scattering angle (°)	Energy (MeV)
1-4	11.21	13.408
5-8	14.84	12.972
9-12	18.34	12.445
13-16	21.71	11.845

Table 3.2: Mean energy of ring groups

Calibration parameters acquired from the preceding analysis were determined for each CsI sector. These parameters were used to fit values of E to the data registered by the CsI ADCs. The gain values for each CsI sector are included in Table 3.3. A

sample calibration plot from CsI sector 12 is shown in Figure 3.4.

CsI Sector	Gain (MeV)
1	9.436
2	9.173
3	10.244
4	9.510
5	10.010
6	9.972
7	10.024
8	12.331
9	9.850
10	8.747
11	9.560
12	11.024
13	9.531
14	9.168
15	10.033
16	9.079

Table 3.3: Gain determined by linear regression

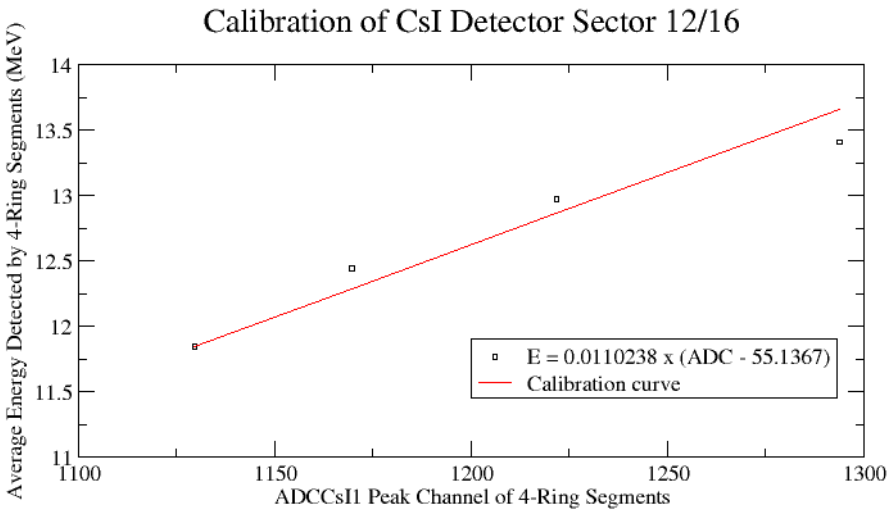

Figure 3.4: Energy calibration of CsI sector 12 using equation (3.1)

It is discussed further in section 4.1 that the pedestal values for each CsI sector were not determined by the aforemention calibration. The value of 55.1367 in units of CsI ADC channels was preset as the pedestal value for every sector based on the

mean offset in ADC. The values of gain displayed in Table 3.3 were then determined by fitting equation (3.1) after setting $ped = 55.1367$. After calibration, the scatterplot of energy detected in CsI versus scattering angle was compared to the kinematics model. Figure 3.5 shows that the experimental data does follow the kinematics model and obeys the relationship between energy and scattering angle outlined in section 3.1.

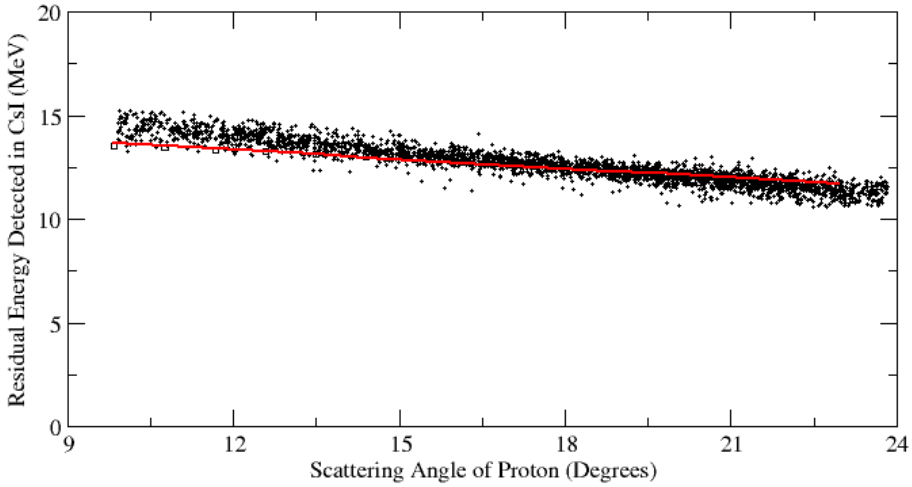

Figure 3.5: Superposition of data and kinematics (θ, E) with a $4.1 MeV/u$ beam

3.3 Inelastic Scattering: Q-Value Resolution

The calibration parameters defined in section 3.2 were used in the analysis of 19 experimental runs with the ^{18}O beam's energy set to 11.8 MeV/u. The higher-energy beam opens up reaction channels for inelastic scattering reactions, which were examined for Q-value resolution. These reactions leave the recoil nucleus in an excited state, with excitation energy equal to the negative of the reaction Q-value. This analysis focuses on the reaction for which the recoil nucleus is in its first excited state ($Q = -1.982$ MeV) [29].

The kinematics model of energy detected in CsI versus scattering angle for the first excited state is compared to the experimental data in Figure 3.6. The band of protons seen above the first excitation band is the elastically scattered protons.

Higher excited states are seen below the modelled band.

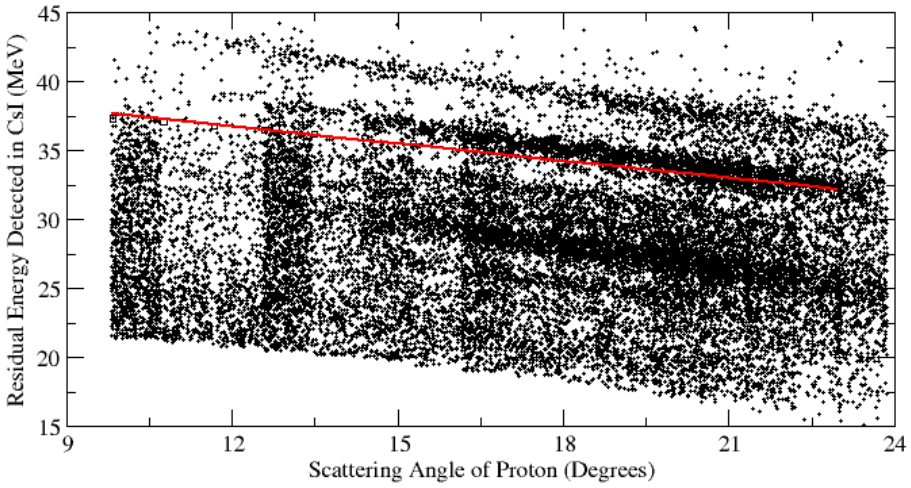

Figure 3.6: Superposition of data and kinematics (θ, E) with the $11.8 MeV/u$ beam

Similar to the first set of data, a scatterplot was generated with ΔE on the vertical axis and the newly calibrated E on the horizontal axis. This plot, shown in Figure 3.7, was centered on the band of protons by comparing it with the kinematics plot of the same variables in Figure 3.8. The inelastic scattering reaction corresponding to the production of the first excited state of ^{18}O was isolated by examining Figure 3.9, a plot of Q versus θ. The Q-value of each CsI sector was then examined individually by breaking up the scattering angles into segments of four rings once again. For each four-ring segment the Q-value was plotted in a histogram, which was fitted with a Gaussian distribution in order to determine the peak Q-value.

In theory, the Q-value for a specific scattering reaction should not depend on the scattering angle. The Q-value in this experiment is determined by the known parameters in Equation (1.1). The angular dependece in Q comes from the energy detected by CsI. The light collection in the associate photodiode may not be the same at different scattering angles, which may influence the recorded energy. The angular variation in Q-value must be fixed so that Q is constant for a given scattering reaction channel.

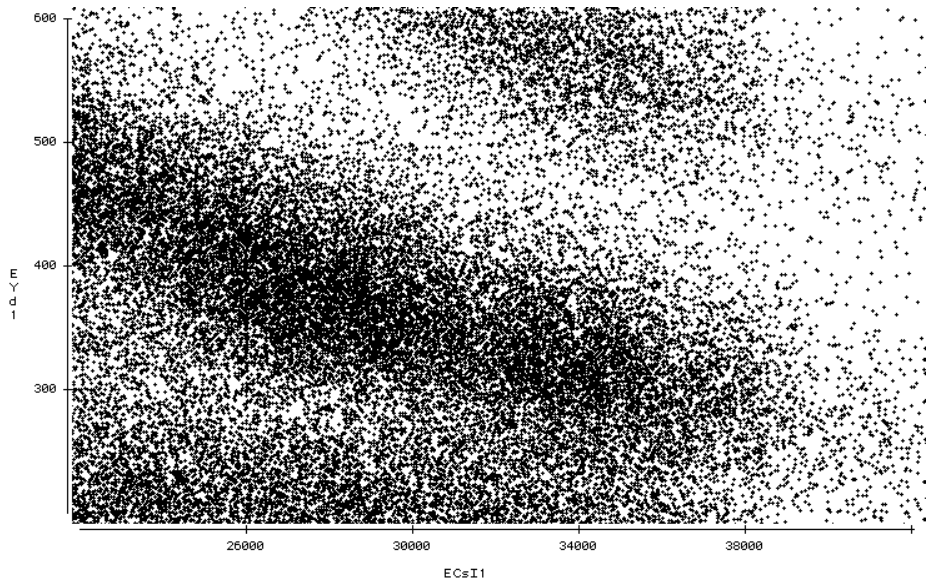

Figure 3.7: Scatterplot of $(E, \Delta E)$ in keV with the $11.8 MeV/u$ beam

The preceding procedures produced four ordered pairs (θ, Q) for each CsI sector, which were plotted and fit with a quadratic regression to model the angular discrepancies in the Q-value. The fit parameters were recorded in Table 3.4. The resulting quadratic equations, $f(\theta)$, were employed in the following calibration equation aimed at correcting the angular variations in Q:

$$Q_{new} = Q - f(\theta) - Ex, \tag{3.4}$$

where Ex is the excitation energy of the reaction channel considered in the quadratic fit. Q_{new} is the best fit to the theoretical Q-value $(-Ex)$, and should give a valid approximation in the consideration of any reaction channel. Equation (3.4) was used to determine a fit for the Q-value for each CsI detector separately. Q_{new} represents the corrected Q-value relative to the aforementioned excitation energy. The corrected plot of Q_{new} versus θ is shown in Figure 3.10.

After analyzing the previous angular fit it was decided that a reaction channel with more data points was needed to fit the low angle portion of the Q-value scatterplot. This was done using a higher excitation state with $Q = -5.255$ MeV [29]. The

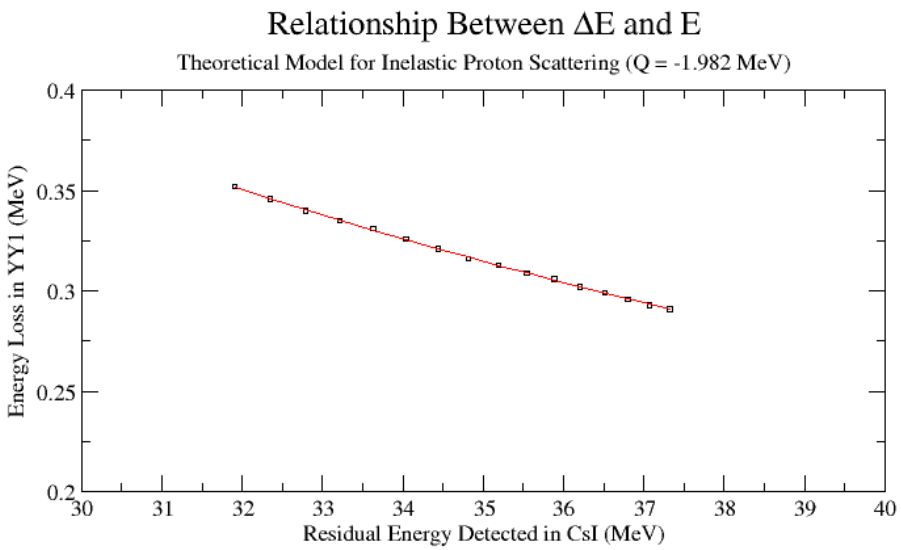

Figure 3.8: Kinematics $(E, \Delta E)$ for $p(^{18}O, p)^{18}O^*$ with the $11.8 MeV/u$ beam

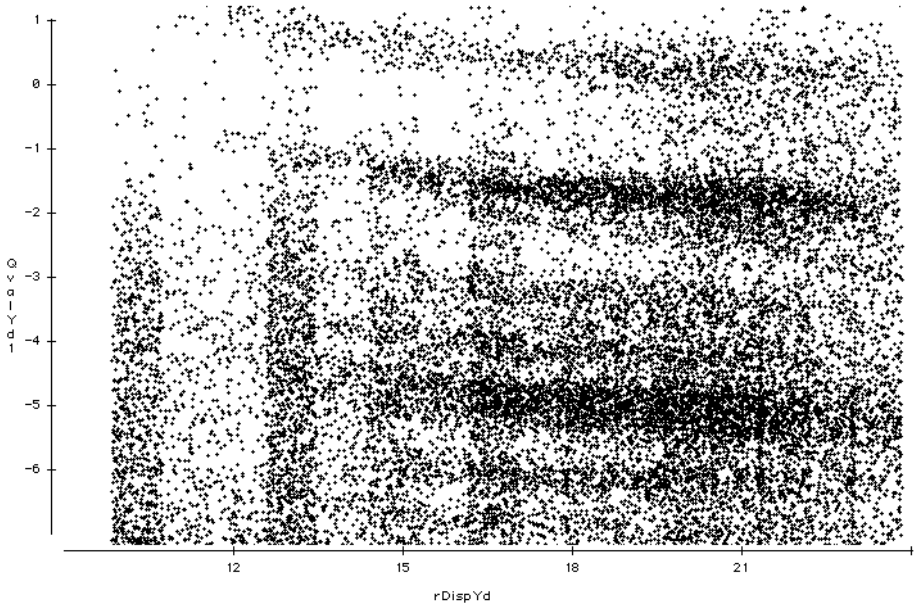

Figure 3.9: Scatterplot of Q-value (keV) versus θ (°)

quadratic fit parameters for this calibration were recorded in Table 3.5. The corrected Q_{new} versus θ plot for this fit is shown in Figure 3.11. This establishes another set of Q_{new} values relative to the higher excitation energy.

CsI Sector	Constant	Coefficient of θ	Coefficient of θ^2
1	-3.1077	0.19428	-0.0060303
2	-6.6293	0.57615	-0.016345
3	0.96055	-0.20792	0.0035647
4	-0.62513	-0.01832	-0.00207
5	-0.36782	-0.054013	-0.00092094
6	-0.070593	-0.100099	0.00048712
7	0.26574	-0.16611	0.0033404
8	1.1923	-0.26766	0.0063313
9	2.5405	-0.43666	0.010819
10	-6.7493	0.58615	-0.016345
11	-6.2098	0.53844	-0.015933
12	2.6738	-0.45747	0.012154
13	-0.44186	-0.086613	0.0010202
14	-2.625	0.14135	-0.0052216
15	0.7912	-0.24731	0.0060454
16	-7.5443	0.56798	-0.013802

Table 3.4: Quadratic fit parameters for $Q = -1.982$ MeV

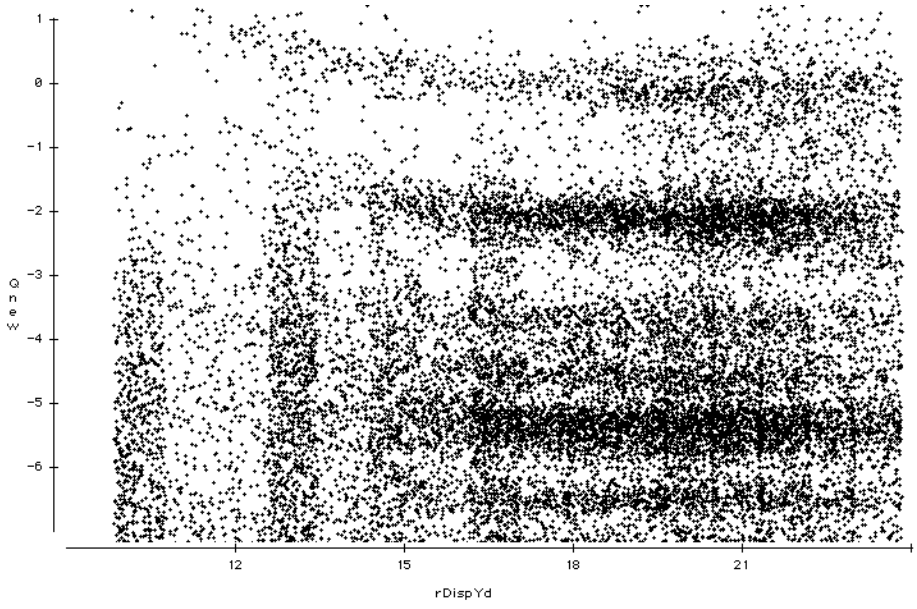

Figure 3.10: Scatterplot of Q_{new} (keV) versus θ $(^\circ)$ after correction

CsI Sector	Constant	Coefficient of θ	Coefficient of θ^2
1	-2.0376	-0.28038	0.006583
2	-2.199	-0.26135	0.0060377
3	-2.4958	-0.22284	0.0046335
4	-3.4488	-0.09658	0.00067656
5	-2.9611	-0.16861	0.0030241
6	-2.6295	-0.2124	0.0042878
7	-1.6144	-0.33752	0.0082297
8	-2.3125	-0.26602	0.0066056
9	-2.2308	-0.26782	0.0059078
10	-2.3714	-0.24623	0.0052674
11	-2.718	-0.21473	0.004568
12	-2.4827	-0.26231	0.0068878
13	-1.4961	-0.35366	0.0086822
14	-0.7022	-0.4448	0.011068
15	-0.9840	-0.44209	0.011841
16	-1.4336	-0.37603	0.0097431

Table 3.5: Quadratic fit parameters for $Q = -5.255$ MeV

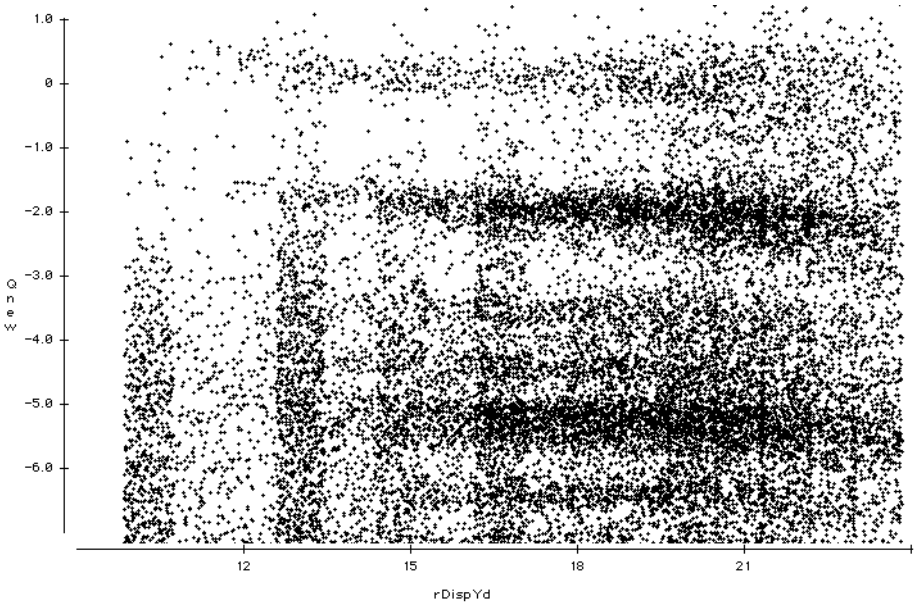

Figure 3.11: Scatterplot of Q_{new} (keV) versus θ $(^\circ)$ after second correction

Qnew (MeV)	Relative to Ex = 1.982 MeV	Relative to Ex = 5.255 MeV
0	0.55	0.63
-1.982	0.54	0.61
-5.255	0.64	0.65

Table 3.6: FWHM resolution in units of MeV for different Q_{new} peaks

After correcting for the angular dependence relative to two different excitation energies, Q_{new} was examined in a histogram for each CsI sector. Each histogram was fitted with a Gaussian distribution in order to identify the peak Q-value and the resolution of the peak. The resolution was given by the full width at half max (FWHM) of the distribution. Values of FWHM were also determined for the entire CsI array. These values are presented for three different peaks in Table 3.6.

Chapter 4

Discussion

4.1 Energy Calibration of CsI

The initial energy calibration was performed using a linear fit to four ordered pairs, in order to characterize the energy E in terms of the ADC signal from each CsI sector. A linear equation for CsI sector 12 is fitted to four data points in Figure 3.4. Although the data were fit with a linear regression, it is evident that there exists some higher order dependence. This may be due in part to the non-uniform light output of the CsI(Tl) scintillator [30].

Table 3.3 displays the value of gain for each sector, which was determined by the slope of the fit line. It was shown in Figure 3.4 that a typical CsI detector did not demonstrate a perfectly linear relationship for this fit. This is demonstrated more noticeably in Figure 3.9, where the angular dependence in Q results in an unbalanced fit around the elastic Q-value line ($Q = 0$) among other reaction channels. The correction for the angular dependence is discussed in section 4.2.

There were a few minor assumptions made during the energy calibration procedure. Firstly, the positions and angles displayed in Table 3.1 do not correspond precisely with the center of each ring. However, the difference was considered to be negligible relative to the energies recorded by the CsI detector. Also, the energy loss in the target was not used in the final calculation of Q-value. This is because the energy loss was deemed too small to be a significant factor in the energy calibration. It was determined that a small distribution offset from these components of the analysis were not comparable to the resolution of the detector.

It was also assumed that using the same pedestal value for each CsI sector was

sufficient for the energy calibration. The pedestal offset was determined by the mean channel of a substantial peak in the histogram of all sectors combined. The mean value was 55.1367; this was used for each CsI after verifying that there were no outliers. By setting the constant, the linear fit was reduced to one degree of freedom. This would be the case even if each sector were given unique pedestal value. There was at most a 2% difference between pedestal values, which relates to a much smaller percentage of the relevant ADC values seen in Figure 3.2. Also, pedestal is defined in ADC channels, which must be an integer number. The value of 55.1367 is based on the best fit instead of actual physical meaning. Using specific, integer pedestal values for each CsI sector may have supported a more accurate calibration fit in the end. However, the differences were minor, and were not significant to the resolution of the detector.

The calibration equation for each sector was determined by the slope of the theoretical energy versus ADC plot, which was fit to only four points. Although data were available for 16 different rings, the sample sizes in individual rings were too small for an accurate plot. After combining the data into groups of four rings there were between 19 and 73 points of data supporting the calculated mean ADC for any one group. This lack of statistics makes it less likely that increasing the number of data points will produce a more accurate fit.

4.2 Angular Correction

The first attempt at an angular Q-value correction was performed using the data from the first excited state ($Q = -1.982$). Similar to the first set of data, there was a very small sample of events recorded for each ring on any one CsI sector. After the data were organized into groups of four rings, several of these groups in the lower angle

range were completely empty, while those in the higher angle range had up to 300 points of data. The mean Q-value was measured for the four outer rings individually if there were less than three ordered pairs for a certain detector. Thus, at least three ordered pairs were available to fit each sector. Figure 4.1 shows a sector with no data from inner ring groups but additional ordered pairs for the rings 13 to 16. An example of a calibration plot with data in each ring group is shown in Figure 4.2.

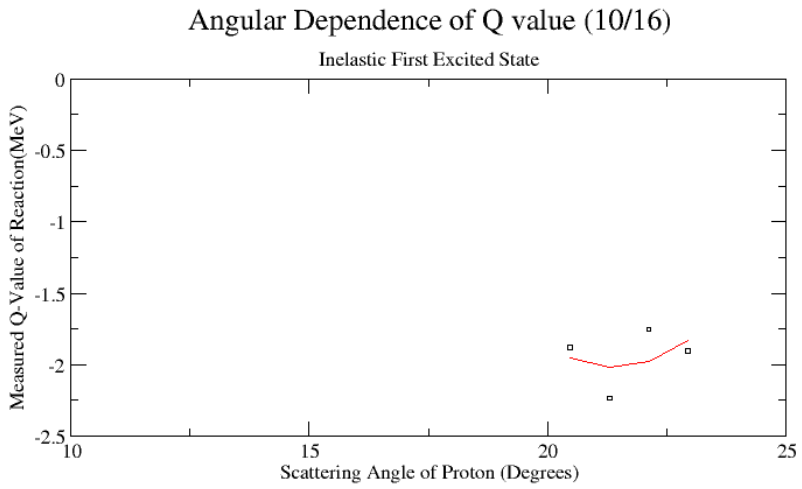

Figure 4.1: Calibration plot with data only from individual rings 13 to 16

It was assumed that the angular dependence in Q could be fit by a polynomial. A quadratic fit was used to model the discrepancy in the Q-value as a function of scattering angle. Although the angular dependence is not necessarily a quadratic, there was not enough data in the low-angle regions to establish an accurate fit. Using a higher order polynomial would cause egregious extrapolations in these regions. These limitations cause some distinct problems in the low-angle regions. Also, the poor statistics may account for some inaccurate fitting equations. Figure 4.1 is an example

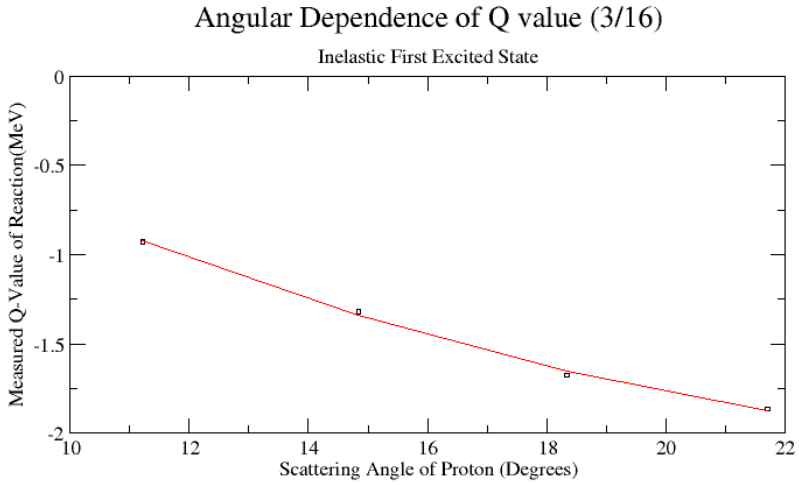

Figure 4.2: Calibration plot using data from four groups of four rings

of an inaccurate fit due to poor statistics. This would cause the corrected Q-value histograms to be skewed or shifted from the theoretical value.

The inelastic Q-value was plotted against scattering angle before any angular correction was applied as seen in Figure 3.9. Ideally the horizontal bands, which represent the Q-value of specific reaction channels, should be flat. A quadratic equation was used to fit the angular dependence and redefine the Q-value accordingly. A. Wagner et al. conducted a similar procedure to account for the position depended output by using a position sensitive $\Delta E - E$ setup [30]. Two Q-value peaks were analyzed for this purpose, producing two different fits.

Compared to the horizontal bands in Figure 3.9, the horizontal bands in the first corrected scatterplot of Q_{new} versus θ (Figure 3.10) are somewhat flatter. A noticeable feature in this plot is the departure from the flat band at lower scattering angles. This is especially prominent in the proton bands associated with elastic scattering ($Q = 0$ MeV) and the first excited state in inelastic scattering ($Q = -1.982$ MeV). Since this fit was calibrated to the data from the first excited state, there was a lack of low-angle data to begin with. This may have produced erroneous curve fitting

Qnew (MeV)	Using $Ex = 1.982$ MeV	Using $Ex = 5.255$ MeV
0	-0.10	-0.01
-1.982	-2.09	-2.02
-5.255	-5.35	-5.29

Table 4.1: Mean Q-value for different Q_{new} peaks

beyond the highly populated regions of the scatterplot.

A different fit was used to correct for the angular dependence of Q in an attempt to elude the problem in the shallow angle region. This fit was completed using the more populous proton band around $Q = -5.255$ MeV. There were enough data in each group to provide four ordered pairs for each CsI sector. The plot of Q_{new} versus θ (Figure 3.11) for this reaction channel does show significant correction in the shallow angle region compared to Figure 3.10. However, it becomes slightly more curved in the very high angle region.

There is an obvious difference in statistics between interior rings and middle to exterior rings. This is likely due to a lower reaction cross section for lower scattering angles. It is shown in Figure 3.9 that there are much fewer points at shallow angles, especially for the elastic and first excited state bands. This caused problems when trying to correct for angular discrepancies in the first, and other excited states.

Performing the angular correction using one reaction channel should have calibrated the CsI detector for any detection along the crystal. Examining the peak Q-value in histograms of other reaction channels should produce expected theoretical values. Both fits for Q_{new} using equation 3.4 proved to have imperfect results. This was mainly apparent at very low or high scattering angles where there was a lack of data. Q-value peaks from different reaction channels were measured using histograms of all CsI sectors combined. These values are displayed in Table 4.1 and compared to their theoretical values on the National Nuclear Data Center (NNDC) website [31]. Columns two and three in Table 4.1 show values of Q_{new} calculated using different values of Ex in Equation (3.4).

Comparing values of both angular corrections from Tables 3.6 and 4.1 shows that the initial fit to the first excited state provides better FWHM resolution values but an inferior fit to the theoretical Q-values. The higher excitation state likely produces closer experimental and theoretical Q-values because it has more data in the shallow angle region, allowing a smoother fit. However, the poor Q-value resolution from this fit indicates that there is still room to improve. A better fit for the angular correction of the Q-value could be achieved by using a different reaction channel. The excited state with $Q = -4.456$ MeV may be a candidate for this fit. It is not as obvious a choice as the more populous bands, but it is still visible and extends with some discernibility into the shallow angle region. Furthermore, it is easily isolated from the background data from other bands. The quality of the fit would improve with the quantity of data provided by additional experimental runs.

4.3 Detector Resolution

The FWHM resolution of the CsI detector array is better for the angular correction to the first excited state. The histogram for the entire CsI array was examined around the $Q = -5.255$ MeV excitation band, the same peak that the angular fit, Equation (3.4), was calibrated to. This histogram, seen in Figure 4.3, seems to show at least three separate peaks between $Q = -5.1$ MeV and $Q = -5.6$ MeV. There should be three different excitation peaks in this range as shown on the NNDC website [31]. However, these excitation peaks do not all have the same strength. Another explanation for this distribution is that all CsI sectors have been combined into one peak, although they may not be calibrated perfectly to one another. It is discussed later that the resolution of individual CsI peaks are better than the resolution for the entire array. This indicates that the angular fit for the calibration to $Ex = 5.255$ MeV is less accurate than the calibration to the first excited state.

In addition to examining the Q-value resolution of the CsI detector as a whole, the

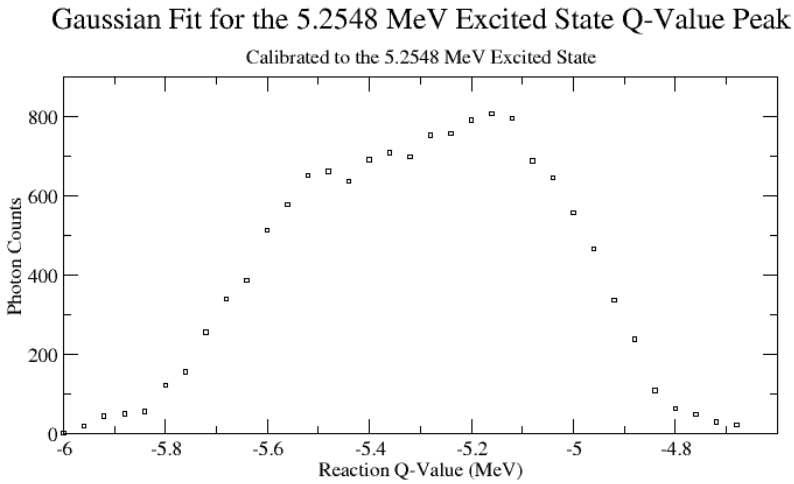

Figure 4.3: Q-value histogram peak near $Q = -5.255$ MeV for the CsI array

resolution of each detector segment was examined in order to identify their individual characteristics. The angular fit to the first excited state was used to plot histograms of Q_{new}. Most histograms of the first excitation energy peak were well populated and provided similar values of resolution. Table 4.2 displays these values along with the number of counts and mean Q-value for each sector. Comparing these values between each sector shows that the angular variations are still very prominent even after the attempt to correct for it. Sector 10, as seen in Figure 4.4, along with neighbouring sectors had Q-value peaks that were significantly shifted from the theoretical value. This fit is not ideal, and it evidently skews many of the plot points in one direction or the other. In sector 3, this manifests as a skewed Gaussian distribution with a tail leaning toward higher energies, see Figure 4.5. In some cases this may indicate irregularities within the CsI sector. However, it is likely just the nature of the fit that brings out the deviations. More strict analysis with a proper angular correction would be needed to identify any major issues with a CsI sector.

Despite the issues surrounding the quadratic angular correction, many sectors provide presentable Gaussian histograms. The histogram for sector 1, seen in Figure

CsI Sector	Event counts	Peak Q-value (MeV)	Q-value resolution (MeV)
1	212	-1.953	0.29
2	112	-2.004	0.43
3	309	-1.866	0.84
4	248	-2.105	0.54
5	259	-2.027	0.41
6	231	-2.144	0.45
7	269	-1.980	0.45
8	238	-1.848	0.60
9	127	-2.313	0.40
10	52	-2.406	0.31
11	213	-2.312	0.38
12	133	-1.809	0.66
13	219	-2.050	0.40
14	182	-2.209	0.43
15	229	-2.078	0.44
16	155	-2.122	0.40

Table 4.2: Q-value histogram data for the first excited state

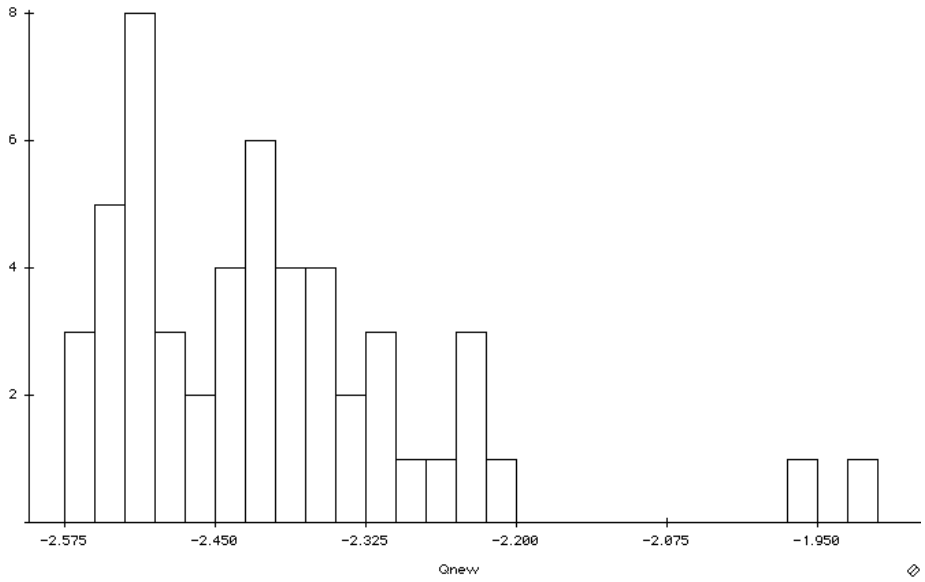

Figure 4.4: Histogram of CsI sector 10 shifted from the $Q = -1.982$ MeV peak

4.6, is an example of this type of distribution. Furthermore, the resolution values of the individual detector sectors are significantly better than those of the CsI detector as a whole. The average resolution value for individual sectors from Table 4.2 is $FWHM = 0.46$ MeV. In comparison, the resolution of the whole detector for the same excited state is $FWHM = 0.54$ MeV., as shown in Table 3.6. This

is understandable because each sector has a different peak and distribution pattern. When plotted in one histogram for the whole detector, the resolving power should decrease. If the angular dependence were corrected properly such that each sector had a Q-value peak similar to the theoretical value, then perhaps the resolution of the entire detector array would improve. Furthermore, the angular correction would reduce the outlying data in each individual sector histogram, reducing the FWHM for each histogram separately.

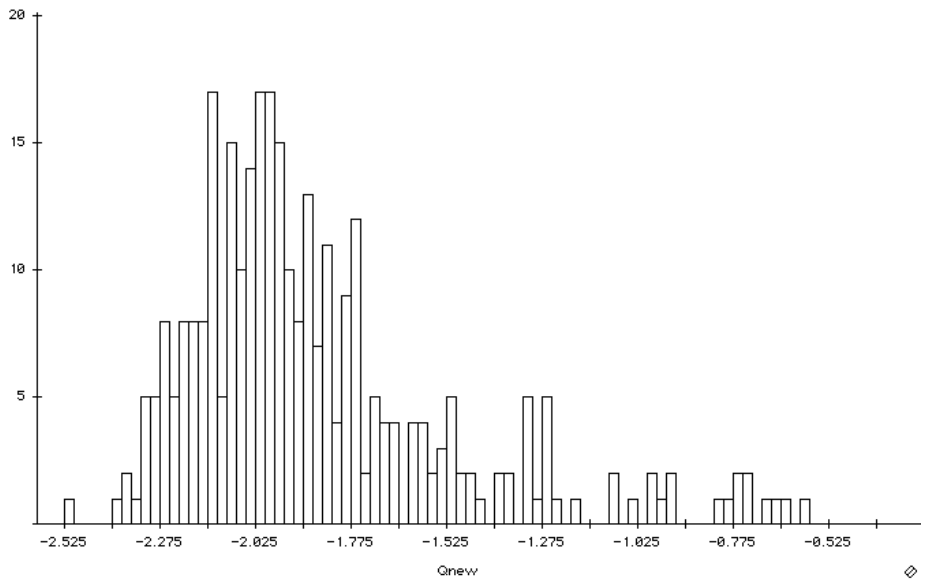

Figure 4.5: Histogram of CsI sector 3 skewed from the $Q = -1.982$ MeV peak

The energy resolution of each CsI sector was measured for different peaks using the 11.8 MeV beam experiment. Figure 4.7 shows values of energy resolution in percentages for the elastic and first excited state peaks of each CsI sector. Sectors with high Q-value resolution from Table 4.2 also show high energy resolution. Sector 8 shows very high energy resolution in the elastic peak. The energy resolution of sector 3 is also an outlier in both peaks. Poor resolution may be attributed to defects in the CsI sectors themselves. There is a lack of data for some sectors in the elastic peak, but most sectors have significant data in the first excited peak to show good resolution.

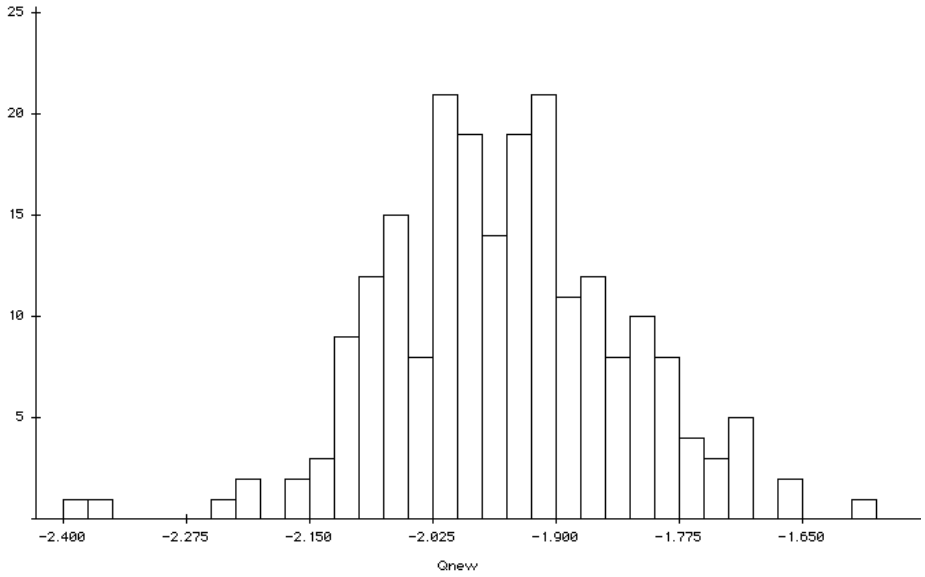

Figure 4.6: Histogram of CsI sector 1 around the $Q = -1.982$ MeV peak

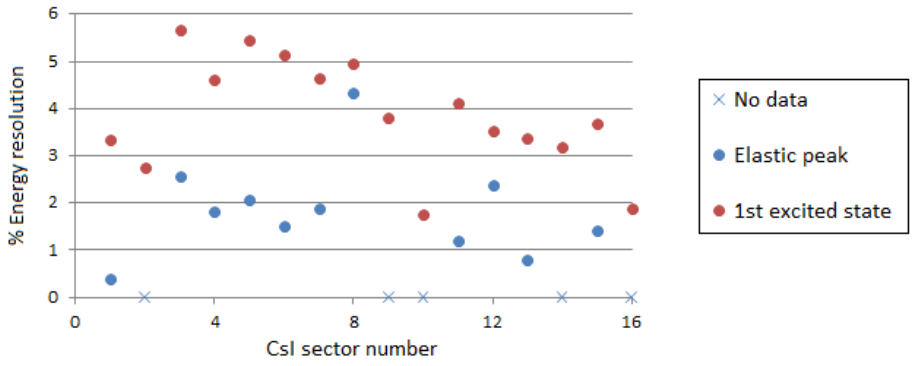

Figure 4.7: Energy resolution of CsI sectors at $Q = 0$ and $Q = -1.982$ MeV peaks

Chapter 5

Conclusions

Data from several experimental runs were analyzed for the characterization of the CsI detector. The linear calibration and angular correction of the Q-value were performed to examine the Q-value resolution of the CsI sectors. The excitation peak at $Q = -1.982$ MeV was found to produce the most accurate angular correction. However, the fit may yet be improved; it did not fit data at small scattering angles as well as it did for moderate scattering angles, which is due to a smaller concentration of data at smaller angles. It was established that interior rings are less likely targets for an event than exterior rings, possibly due to a smaller reaction cross section. The calibration showed that the average Q-value peaks for the CsI array were slightly shifted from the theoretical values (see Table 4.1). Some individual CsI sectors were shifted significantly from the theoretical value.

The Q-value resolution of the CsI detector was determined to be 0.54 MeV for the first excited state with small variances depending on the Q-value peak and the angular correction used. The average resolution for individual CsI sectors is significantly better at 0.46 MeV. If an improved fit is used to correct the angular dependence this resolution is expected to improve further. The Q-value and energy resolution of most CsI sectors were consistent, but sectors 3 and 8 were identified with higher resolution. These outliers may require further inspection to verify that all sectors provide accurate results in further experimentation.

Acknowledgements

I would like to thank my supervisor, Dr. Rituparna Kanungo, for organizing this study and guiding me through this experience. I greatly appreciate the dedication and hard work of all members of the IRIS team who took part in the collection of the data for this study. I am grateful to have taken part in the IRIS project as well. I also thank my family and friends for their support, encouragement, and proofreading expertise. Lastly, I thank and acknowledge the support of Saint Marys University and TRIUMF as well as the following institutions for their contributions to funding the IRIS project: CFI, NSRIT, NSERC.

Bibliography

[1] Thielemann et al. Nuclear physics issues of the r process. New Jersey [u.a.], S. 311, (2002)

[2] I. Tanihata. Neutron halo nuclei. Journal of Physics, G: Nuclear and Particle Physics, 22, 157, (1996)

[3] K. Riisager. Halos and related structure. Physica Scripta, T152, 014001, (2013)

[4] A.V. Dobrovolsky et al. Study of the nuclear matter distribution in neutron-rich Li isotopes. Nuclear Physics A766, 1, (2006)

[5] I. Tanihata et al. Recent experimental progress in nuclear halo structure studies. Progress in Particle and Nuclear Physics 68, 215, (2013)

[6] R. Kanungo. A new view of nuclear shells. Physica Scripta, T152 014002 (2013)

[7] I. Tanihata. RI beams dream and reality. Nuclear Physics, A4685, 80, (2001)

[8] A.H. Wuosmaa et al. A solenoidal spectrometer for reactions in inverse kinematics. Nuclear Instruments and Methods in Physics Research, A 580, 1290, (2007)

[9] R. Kanungo, IRIS proposal, private communication

[10] Richard A. Dunlap. An Introduction to the Physics of Nuclei and Particles, Brooks/Cole, CA. (2003)

[11] Meyer et al. *R*-process nucleosynthesis in the high-entropy supernova bubble. The Astrophysical Journal, 399, 656, (1992)

[12] Teresawa et al. New nuclear reaction flow during r-process nucleosynthesis in supernovae: critical role of light, neutron-rich nuclei. The Astrophysical Journal, 562, 470, (2001)

[13] Charignon. An r-process code and graphical user interface for heavy-element nucleosynthesis. Astronomy & Astrophysics, 531, A79 (2011)

[14] Meyer. Neutrino reactions on ^{4}He and the r-process. The Astrophysical Journal, 449, 55, (1995)

[15] Glenn F. Knoll, Radiation Detection and Measurement, NJ: Wiley, p31, (2010)

[16] P.F. Mastinu et al. Calibration of CsI(Tl) scintillators for heavy ions ($3 \leq Z \leq 54$) in a wide energy range (E/u $\leq$ 60 MeV/u). Nuclear Instruments and Methods in Physics Research, A 338, 419, (1994)

[17] R. Lozeva et al. Investigation of scintillation detectors for relativistic heavy ion calorimetry. Nuclear Instruments and Methods in Physics Research, B 204, 678, (2003)

[18] A.S. Fomichev et al. The response of a large CsI(Tl) detector to light particle and heavy ions in the intermediate energy range. Nuclear Instruments and Methods in Physics Research, A 344, 378, (1994)

[19] W.G. Gong et al. Resolution tests of CsI(Tl) scintillators read out by PIN diodes. Nuclear Instruments and Methods in Physics Research, A268, 190, (1988)

[20] G. Ren et al. Non-uniformity of light output in large-sized CsI(Tl) crystals grown by non-vacuum Bridgman method. Nuclear Instruments and Methods in Physics Research, A 564, 364, (2006)

[21] Bicron (Saint-Gobain), 12345 Kinsman Rd., Newbery, OH 44065, USA

[22] Hamamatsu Photonics: http://www.hamamatsu.com/jp/en/product/category/3100/4001/41
08/index.html

[23] TRIUMF, ISAC Facilities Page: http://www.triumf.ca/research-program/research-facilities/isac-facilities

[24] TRIUMF, Main Cyclotron Page: http://www.triumf.ca/research-program/research-facilities/main-cyclotron-beam-lines

[25] Micron Semiconductor LTD, 1 Royal Buildings, Marlborough Road, Lancing, Sussex BN158UN, England

[26] L. Tassan-Got. A new functional for charge and mass identification in $\Delta E - E$ telescopes. Nuclear Instruments and Methods in Physics Research, B 194, 503, (2002)

[27] Catkin Kinematics Calculator: http://personal.ph.surrey.ac.uk/ phs1wc/kinematics/

[28] LISE++ Spectrometry Calculator: http://lise.nscl.msu.edu/lise.html

[29] D. R. Tilley et al. Energy levels of light nuclei $A = 18 - 19$. Nuclear Physics A595, 1 (1995)

[30] A. Wagner et al. Energy resolution and energy light response of CsI(Tl) scintillators for charged particle detection. Nuclear Instruments and Methods in Physics Research, A 456, 290, (2001)

[31] National Nuclear Data Center: http://www.nndc.bnl.gov/